Enhancement of High Temperature Strength of 2219 Alloys Through Small Additions of Nb and Zr and a Novel Heat Treatment

S. MONDOL, S.K. MAKINENI, S. KUMAR, and K. CHATTOPADHYAY

This paper presents a detailed investigation on the effect of small amount of Nb and Zr additions to 2219 Al alloy coupled with a novel three-stage heat treatment process. The main aim of the work is to increase the high temperature strength of 2219 alloy by introducing thermally stable $L1_2$ type ordered precipitates in the matrix as well as by reducing the coarsening of metastable strengthening θ'' and θ' precipitates. To achieve this, small amounts of Nb and Zr are added to 2219 alloy melt and retained in solid solution by suction casting in a water-cooled copper mould having a cooling rate of 10^2 to 10^3 K/s. The suction cast alloy is directly aged at 673 K (400 °C) to form $L1_2$ type ordered coherent Al_3Zr precipitates. Subsequently, the alloy is solution treated at 808 K (535 °C) for 30 minutes to get supersaturation of Cu in the matrix without significantly affecting the Al_3Zr precipitates. Finally, the alloy is aged at 473 K (200 °C), which results in the precipitation of θ'' and θ'. Microstructural characterization reveals that θ'' and θ' are heterogeneously precipitated on pre-existing uniformly distributed Al_3Zr precipitates, which leads to a higher number density of these precipitates. This results in a significant increase in strength at room temperature as well as at 473 K (200 °C) as compared to the 2219 alloy. Furthermore, the alloy remains thermally stable after prolonged exposure at 473 K (200 °C), which is attributed to the elastic strain energy minimization by the conjoint Al_3Zr/θ' or Al_3Zr/θ'' precipitates, and the high Zr and Nb solute-vacancy binding energy, retarding the growth and coarsening of θ'' and θ' precipitates.

https://doi.org/10.1007/s11661-018-4614-3

I. INTRODUCTION

HEAT-TREATABLE AL alloys have drawn a great deal of attention due to their advantages for structural applications in the automobile and aerospace industries.[1] The 2XXX series Al alloys, which are strengthened by the formation of precipitates, are some of the most studied age-hardenable alloy systems. The precipitation sequence of this alloy is accepted to occur as follows: Supersaturated solid solution (SSSS) → Guinier–Preston (GP) zones → θ'' (GPII zones) → θ' → equilibrium θ.[2] The strength of the alloy is controlled by the metastable θ'' and θ' precipitates. Therefore, it is necessary to introduce new precipitates in the Al matrix or modify the precipitation kinetics of the existing precipitates for further improvement of strength of the alloy at room temperature as well as at elevated temperature.

The addition of small amounts of transition metals, such as Sc, Zr, Nb, Hf, V, Ti *etc*., as micro alloying elements to age-hardenable Al alloys can form stable or metastable $L1_2$ type trialuminides, which makes a distinct positive effect on room temperature as well as high temperature strength of the alloy.[3–8] Moreover, the addition of these elements in Al-Cu- and Al-Mg-based alloys can refine the grain size and morphology, and improve recrystallization resistance.[9–16]

In the present investigation, Zr and Nb are added to the commercial 2219 alloy to improve its high temperature mechanical properties. Zr has solid solubility of about 0.29 wt pct in Al at the peritectic temperature of 933.8 K (660.8 °C).[17] In Al-Zr binary alloy, nanometre-sized Al_3Zr precipitates with metastable $L1_2$ structure form during aging in the temperature range of 648 K to 698 K (375 °C to 425 °C).[18,19] These $L1_2$ precipitates transform to the equilibrium DO_{23} phase after prolonged aging at a temperature above 698 K (425 °C).[19–22] Although these precipitates have a larger size, they are stable and remain coherent due to the small lattice mismatch with Al (+ 0.75 pct).[23–25] Stability of these $L1_2$ precipitates arises from slower

S. MONDOL, S.K. MAKINENI, S. KUMAR and K. CHATTOPADHYAY are with the Department of Materials Engineering, Indian Institute of Science, Bengaluru 560012, India. Contact e-mail: kamanio@materials.iisc.ernet.in
Manuscript submitted April 18, 2017.
Article published online May 1, 2018

diffusivity of Zr in Al and coherency due to small lattice parameter mismatch of Al_3Zr with Al.[3,18,26] Moreover, the addition of Zr improves creep resistance and thermal stability of Al alloys at elevated temperatures.[3,4,27]

The solid solubility of Nb in Al is 0.22 wt pct at the peritectic temperature of 913 K (640 °C), decreasing to less than 0.1 wt pct at 573 K (300 °C). The diffusivity of Nb in Al is also very low.[3,28] Addition of Nb to Al or Al alloy forms equilibrium DO_{22} type Al_3Nb intermetallic. This DO_{22} crystal structure is stable at high temperature but is very brittle in nature. A few studies have reported the formation of metastable Ll_2 structure in Al-Nb alloy.[3,29] $L1_2$ type Al_3Nb dispersoids can be obtained by applying controlled cooling with a cooling rate greater than 10^3 K/s.[30,31]

The $L1_2$ type Al_3Zr particles are known to precipitate discontinuously in Al-Zr alloys.[32] This discontinuous precipitation can be suppressed by tuning the lattice misfit through suitable alloying additions such as Ti, V, Nb *etc*.[33–36] Chuang and Tu reported that the addition of Nb to an Al-Cr-Zr alloy lowered the misfit strain and interfacial energy, and resulted in uniform precipitation of $L1_2$ type Al_3Zr particles in Al matrix.[33] They also reported that the addition of Nb improves the thermal stability of the alloy due to the partitioning of Nb in the $L1_2$ type Al_3Zr particles resulting in the formation of $L1_2$ type Al_3(Zr, Nb) particles.[33] Additionally, with Nb addition in the order of 0.10 wt pct or more, a significant grain refinement can be achieved.[9]

It has been established by our research group that the trace amount of alloying additions and a new heat treatment process can cause a significant increase in room temperature and elevated temperature strength of a binary Al-Cu alloy.[37,38] A part of that work included preparing an Al-4.5 wt pct Cu-0.33 wt pct Nb-0.48 wt pct Zr alloy by suction casting in a water-cooled copper mold at a cooling rate in the range of 10^2 to 10^3 K/s. The cast alloy was subsequently processed using a novel three-stage heat treatment process. The process route followed was Arc melting → chilled copper mould casting → aging at 673 K (400 °C), 10 hours → solutionising at 808 K (535 °C), 30 minutes → aging at 463 K (190 °C). It was observed that 0.2 pct proof stress (PS) was 460 ± 18 MPa at room temperature and 250 ± 16 MPa at 523 K (250 °C) after peak aging at 463 K (190 °C), which is extremely good and has been patented and published.[38,39] Microstructural analysis revealed that the significant improvement of yield strength at room temperature as well as at elevated temperature was due to the formation of stable coherent $L1_2$ type Al_3Zr precipitates and θ'' precipitates, where the heterogeneous nucleation of θ'' precipitates on Al_3Zr precipitates led to slower growth and coarsening kinetics of the precipitates and better high temperature properties.

This paper focuses on studying the effect of the similar addition of Zr and Nb to the commercial 2219 alloy (designated henceforth as 2219NbZr alloy) using a similar three-stage heat treatment route. The impact of this novel three-stage heat treatment process on the microstructural modification and mechanical properties of 2219NbZr alloy are evaluated through extensive microstructural and mechanical characterization, and by correlating the microstructural characteristics after each stage of processing with the tensile properties.

II. EXPERIMENTAL PROCEDURE

For the present investigation, 0.33 wt pct Nb (99.9 wt pct) and 0.33 wt pct Zr (99.9 wt pct) are added to the commercial 2219 alloy, since 2219 alloy already contains 0.15 wt pct Zr. The chemical composition in wt pct of the commercial 2219 alloy and 2219NbZr alloy is given in Table I. The alloy is prepared in the form of 10 g buttons by arc melting. These are melted several times to obtain compositional homogeneity. Subsequently, the buttons are suction cast in a water-cooled copper mold in the form of strips having 3 mm thickness and 10 mm width. The cooling rate for this process is in the range of 10^2 to 10^3 K/s.

The suction cast alloy is aged at 673 K (400 °C) to form Al_3Zr precipitates. Subsequently, the alloy is solution treated at 808 K (535 °C) for 30 minutes to increase the Cu concentration in solid solution without significantly affecting the already formed Al_3Zr precipitates. This is followed by a second-stage aging treatment at 473 K (200 °C) to precipitate θ'' and θ' precipitates.

The grain morphology is studied using scanning electron microscopes (SEM) and the grain size is measured by electron backscatter diffraction (EBSD) mapping. The precipitation behavior is characterized by transmission electron microscope (TEM). Bulk composition analysis is performed using electron probe micro-analyzer (EPMA) and composition of the nanometer-sized precipitates is analyzed using TEM-EDS. TEM observations are conducted on a JEOL 2000FX microscope operated at 200 kV and an FEI TEM system fitted with energy dispersive X-ray spectroscopy (EDS) analysis operating at 300 kV.

After each processing step, hardness is measured and tensile properties at room temperature as well as at 473 K (200 °C) are measured after peak aging of the alloy. Vickers hardness measurements are made on a Zwick Roell ZHV1-A Vickers micro-hardness tester. The tensile tests are conducted on Instron 5967 at a strain rate of 10^{-3} s^{-1}. Micro-tensile samples of 6 mm gauge length and 0.5 mm thickness are used for the experiments. For each condition, minimum four samples are tested and the average values are reported.

III. RESULTS AND DISCUSSION

A. *Suction Casting*

After casting of the 2219NbZr alloy, the Vickers micro-hardness of the cast structure is found to be 844 ± 29 MPa along the longitudinal section as well as the transverse section. SEM micrographs of the suction cast samples are shown in Figure 1(a). It is observed that the as-cast microstructure of the alloy exhibits equiaxed grains. Grain size is measured using EBSD

analysis (Figure 1(b)) and is found to be 30 ± 10 μm. The grain size of the commercial 2219 alloy processed in the similar manner is found to be 66 ± 7 μm. Thus, the presence of Nb and Zr in the alloy helps to refine grain size. It has also been reported in the literature that the peritectic-forming solutes, such as, Nb, Zr, V, Ti, have remarkable effect on the refinement of grain size of Al alloys.[9] In our alloy, few petal-shaped particles could also be observed inside the grains, as shown in the inset of Figure 1(a). The compositional analysis of these particles and the distribution of Nb and Zr are determined by EDS and WDS elemental mapping using EPMA. The composition of the petal-like particles is found to be close to Al_3Zr and the composition of the grain boundary phase is close to θ (Al_2Cu) phase. It is found that the matrix contains 1.6 ± 0.3 wt pct Cu. Zr concentration is 0.32 ± 0.1 wt pct in the matrix and 0.17 ± 0.1 wt pct in the grain boundary phase. The concentration of Nb is 0.4 ± 0.1 wt pct in the matrix and less than 0.1 wt pct in the grain boundary phase. Elemental mapping of 2219NbZr alloy is shown in

Table I. Chemical Composition of the Alloys (Weight Percent)

	Al	Cu	Zr	Nb	Mn	V	Ti	Si	Fe
2219 (Base Alloy)	bal.	6.5	0.15	—	0.32	0.06	0.03	0.05	0.13
2219NbZr	bal.	6.5	0.48	0.33	0.32	0.06	0.03	0.05	0.13

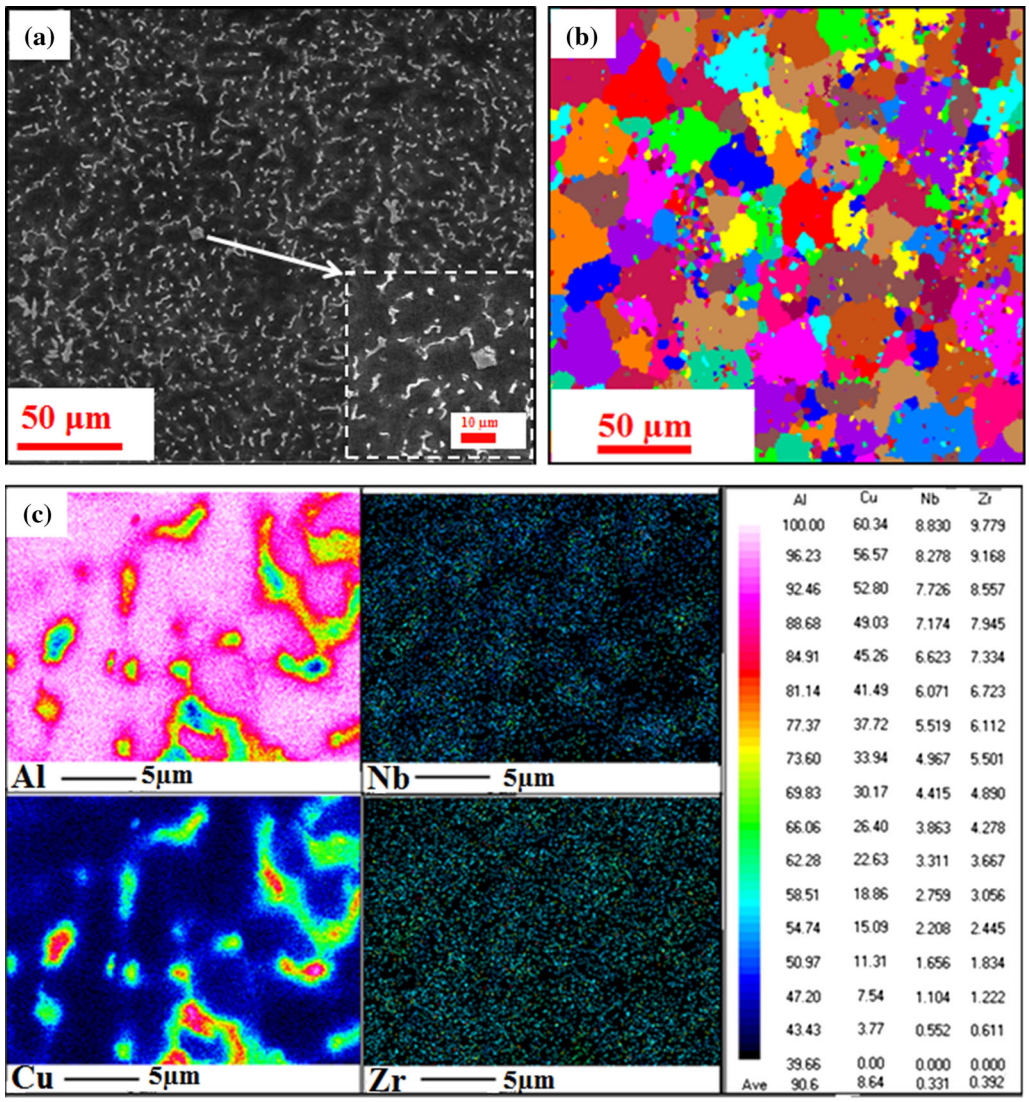

Fig. 1—Suction cast 2219NbZr alloy (*a*) SEM micrograph exhibiting equiaxed grains and a petal-like primary Al_3Zr particle inside a grain shown in the inset, (*b*) EBSD image showing the grain size distribution, and (*c*) WDS elemental mapping showing the elemental distribution.

Figure 1(c). It reveals uniform dispersion of Nb and Zr in the matrix.

B. *Artificial Aging at 673 K (400 °C)*

After casting, the first stage of aging of the 2219NbZr alloy is carried out at 673 K (400 °C) followed by water quenching. The aging curve is shown in Figure 2. The hardness of the alloy increases with time up to 10 hours of aging after which it reaches a plateau. The peak aged sample (10 hours) exhibits a hardness value of 1101 ± 23 MPa. Thus, peak aging at 673 K (400 °C) leads to an increase in the hardness of 267 MPa.

To understand the cause of the increase of hardness, TEM analysis is performed for the peak aged sample. SAD patterns along $[001]_{Al}$, $[011]_{Al}$, and $[112]_{Al}$ zone axes are shown in Figures 3(a) through (c). It is observed that the superlattice spots are present in all the diffraction patterns. These superlattice reflections confirm the formation of $L1_2$ type ordered precipitates. The dark-field image corresponding to the encircled superlattice spot along $[001]_{Al}$ zone axis is shown in Figure 3(d). Very fine, uniformly distributed and closely spaced precipitates are observed in the dark-field image. The size distribution curve for these precipitates is presented in the inset of the dark-field image. The precipitates have a narrow size distribution in the range 1.5 to 4 nm with an average size of 2.3 ± 0.5 nm (radius). To provide a clearer picture a HRTEM image of $L1_2$ precipitates is shown in Figure 3(e). In order to get a qualitative idea about the chemistry of $L1_2$ precipitates, STEM mapping image is shown in Figure 3(f), which reveals that the precipitates are enriched in Zr. Furthermore, EDS analysis using STEM nanoprobe reveals that the composition of the $L1_2$ precipitates is Al-23.6Zr-2.4Cu-0.15Nb (in at. pct), which is close to Al_3Zr. The results do not reveal much Nb partitioning in Al_3Zr precipitates. The previous study of Al-Cu-Nb-Zr alloy by Makineni *et al.* in our group has also reported the composition of these $L1_2$ type ordered precipitates through Atom Probe Tomography analysis as Al-22Zr-2.03Cu-0.5Nb (in at. pct), which is close to the stoichiometry of Al_3Zr with minor amounts of Cu and Nb replacing Zr.[38] Thus, any significant Nb partitioning in Al_3Zr precipitates as

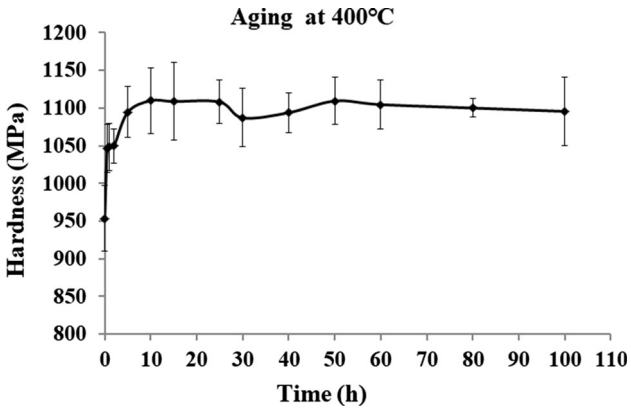

Fig. 2—Aging curve of 2219NbZr alloy at 673 K (400 °C).

observed by Chuang and Tu[33] was not observed in the experiments conducted in our group. It could be due to the much higher amount of

Nb in the alloy and much higher cooling rate employed in their work. Thus, the main role of Nb in our work is to prevent discontinuous precipitation of Al_3Zr precipitates. The strength increase after first stage of aging originates from these $L1_2$ type ordered Al_3Zr precipitates.

C. *Solution Treatment at 808 K (535 °C)*

Solution treatment time at 808 K (535 °C) was optimized by measuring hardness value of the alloy for different solution treatment times by our group.[37] The hardness *vs* time plot at this temperature for the Al-4.5Cu-0.33Nb-0.48Zr (wt pct) alloy is shown in Figure 4(a). This graph indicates that the hardness of the alloy drastically decreases after 30 minutes of solution heat treatment due to rapid coarsening of Al_3Zr precipitates. Therefore, after aging at 673 K (400 °C), the 2219NbZr alloy is solution treated at 808 K (535 °C) for 30 minutes. It is found that this leads to an increase in Cu concentration in the matrix to 4.1 ± 0.5 wt pct. Figure 4(b) shows the elemental mapping for the solution-treated alloy. It is observed that a part of the grain boundary phase (θ) remains undissolved, and Nb and Zr are present inside the grain. The presence of Nb and Zr probably restricts the diffusion of Cu in the matrix, hence less enrichment of Cu in the matrix takes place and some undissolved θ phase remains at the grain boundary.

The dark-field image and SAD pattern along $[001]_{Al}$ zone axis is shown in Figure 4(c). Superlattice spots corresponding to $L1_2$ type ordered structure are observed in the SAD pattern. From the SAD pattern it can be confirmed that after solution treatment Al_3Zr precipitates do not undergo structural transformation. The dark-field image shows these to be Al_3Zr precipitates, which remain unaffected by solution treatment. Size distribution analysis of these precipitates has been carried out after peak aging at 473 K (200 °C) as it is assumed that 473 K (200 °C) is a too low a temperature for any change in the size and distribution of Al_3Zr precipitates. The solution-treated alloy results in a hardness of 1076 ± 23 MPa, which is very close to the peak hardness value obtained after 673 K (400 °C) aging.

D. *Artificial Aging at 473 K (200 °C)*

The solution-treated samples are kept at 473 K (200 °C) for second-stage aging. The variation of micro-hardness with time is shown in Figure 5. The hardness increases rapidly up to 10 hours of aging and yields a maximum value of 1445 MPa. Following this, the hardness drops gradually up to 25 hours and reaches a plateau.

TEM analysis has been carried out to study the precipitation behavior of the alloy after 10 hours peak aging at 473 K (200 °C). SAD pattern along $[001]_{Al}$ zone axis is shown in Figure 6(a) and a schematic

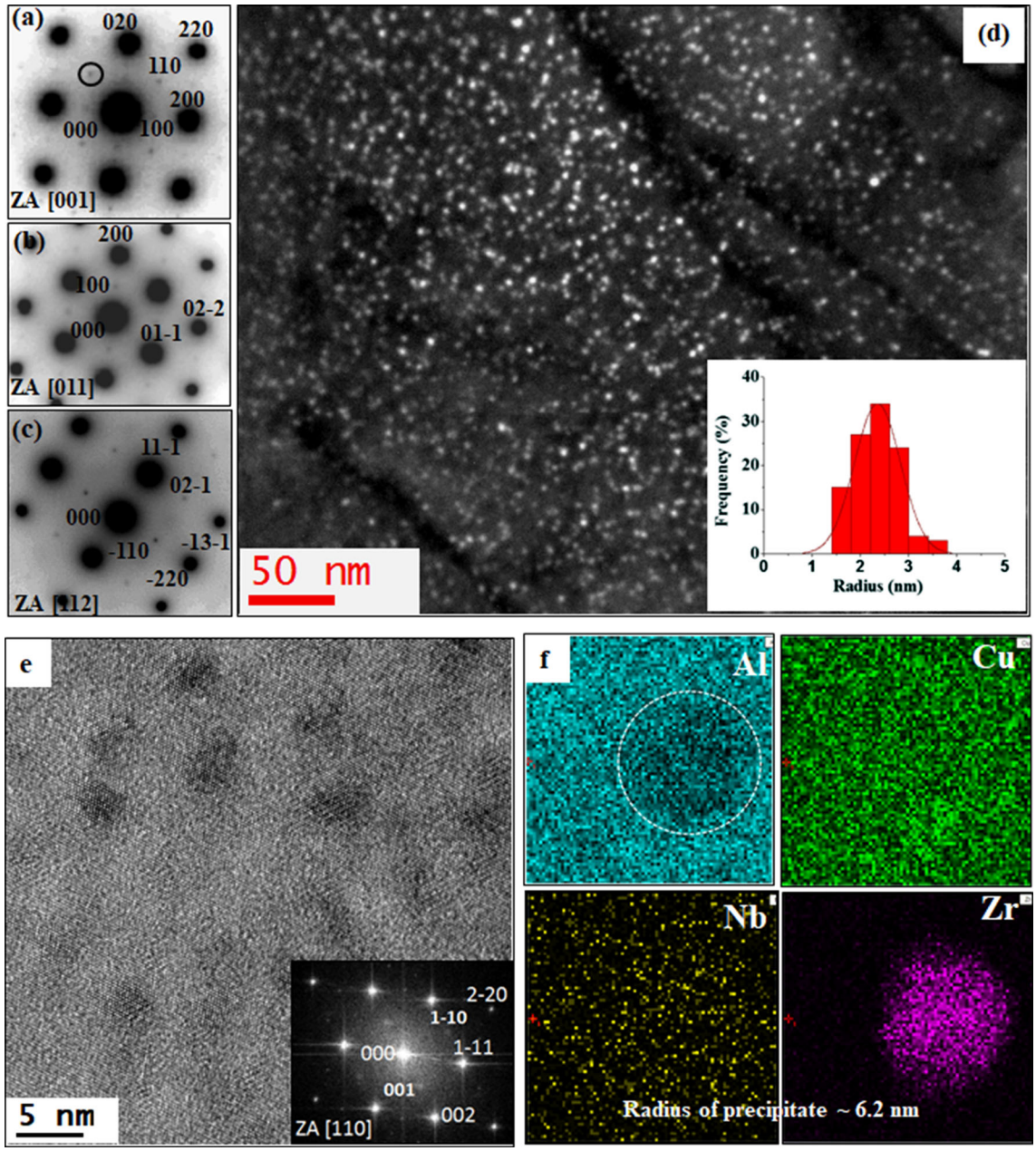

Fig. 3—2219NbZr alloy aged at 673 K (400 °C) for 10 h (*a*) SAD patterns along $[001]_{Al}$, (*b*) $[011]_{Al}$, (*c*) $[112]_{Al}$, and (*d*) dark-field image taken near to $[001]_{Al}$ zone axis with $\bar{1}10$ superlattice ordered spot reflecting Al_3Zr precipitates with inset showing precipitate size distribution histogram, (*e*) HRTEM image and (*f*) STEM EDS mapping of Al_3Zr precipitates.

diagram of the marked area of the SAD pattern is shown in Figure 6(b) for clarity. The SAD pattern exhibits streaks, characteristic of coherent θ'' precipitates with intensity maxima at ¼, ½, and ¾ of the reciprocal lattice position of the {200} reflections, as well as reflections at {100} and {110} positions that correspond to the $L1_2$ ordered structure. Reflections corresponding to θ' precipitates are also observed in the SAD pattern, as marked in Figure 6(b). Figure 6(c) shows the dark-field micrograph corresponding to the encircled reflection in the SAD pattern. The dark-field image reveals that the microstructure consists of $L1_2$ ordered Al_3Zr, θ'' and θ' precipitates. The nature of distribution and size of θ'' and θ' precipitates are determined from several bright-field, dark-field, and HRTEM images.

The Al_3Zr precipitates are spherical in nature with faceted interface. However, presence of faceted interface is not clearly observed for all the Al_3Zr precipitates. It is found that the precipitates with larger radii are faceted along {100} and {110} planes. As an example, an inverse FFT image of an Al_3Zr precipitate along $[100]_{Al}$ zone axis is shown in Figure 7(a). It is observed that this precipitate has octagonal shape with $\{100\}_{ppt}$ and $\{110\}_{ppt}$ faceting planes, as exhibited in the schematic diagram shown in the same figure. The size distribution curve, shown in Figure 7(b), reveals that the variation in

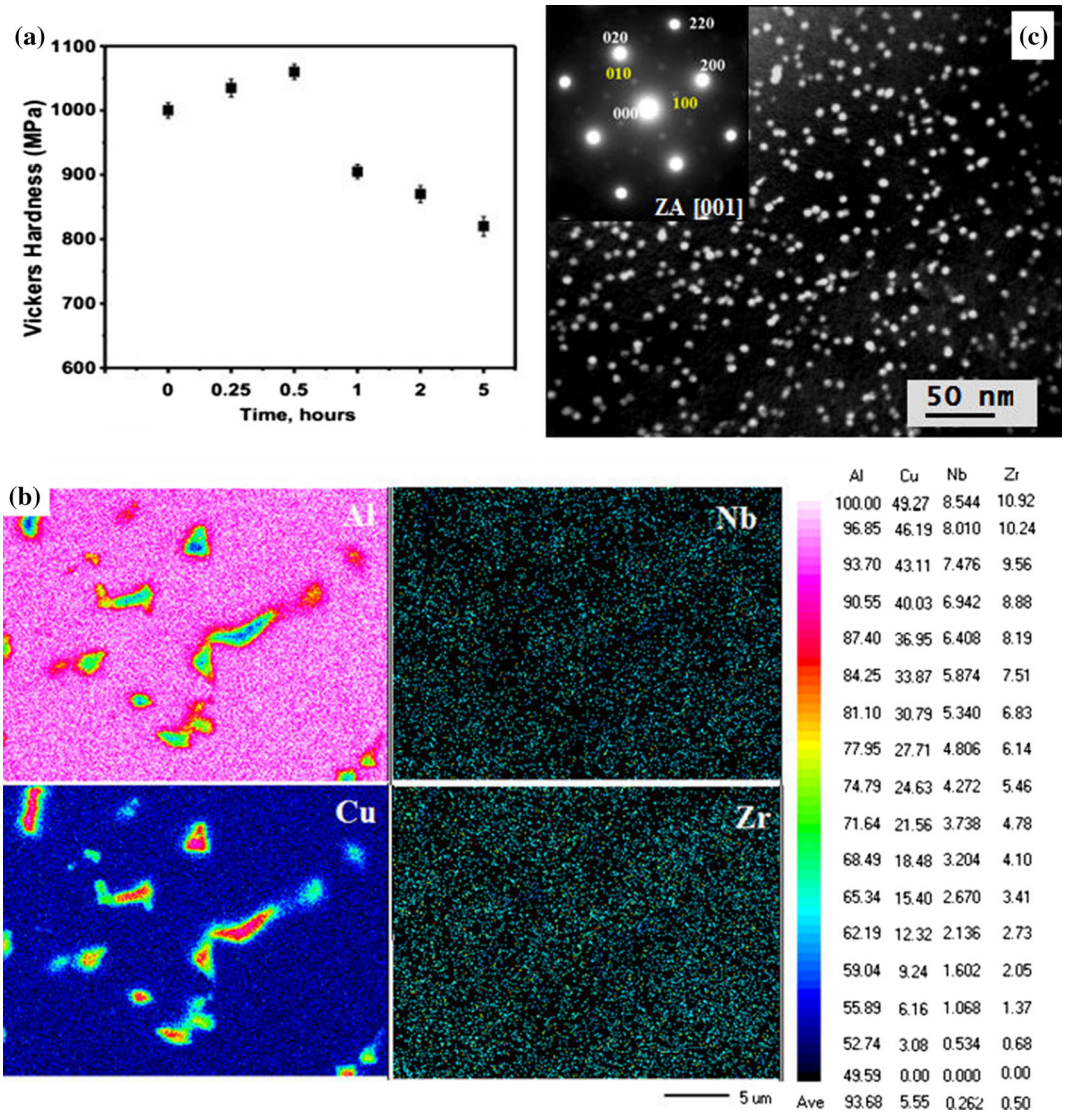

Fig. 4—Solution treatment at 808 K (535 °C). (*a*) Vickers hardness *vs* solution treatment time for Al-Cu-Nb-Zr alloy, (*b*) WDS elemental mapping showing the distribution of Al, Cu, Nb, and Zr for 2219NbZr alloy after 30 min of solution treatment, and (*c*) dark-field image taken near to $[001]_{Al}$ zone axis using a superlattice ordered 100 spot and the corresponding SAD pattern shown as an inset for 2219NbZr alloy after 30 min of solution treatment.

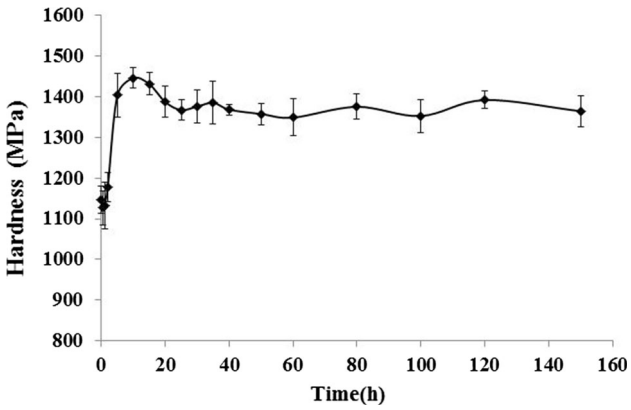

Fig. 5—Aging curve of 2219NbZr alloy at 473 K (200 °C).

size of the precipitates is larger compared to that of the precipitates after first stage of aging shown in Figure 3(d). These precipitates have a size range of 2.1 to 7 nm with an average size of 4.7 ± 1.4 nm (radius) and are homogenously distributed throughout the matrix.

A representative HRTEM image along $[100]_{Al}$ zone axis and the FFT corresponding to the plate-like precipitates are shown in Figure 7(c). The characteristic reflections of θ' precipitates observed in the FFT confirm that the plate-like precipitates are θ'. It is observed that θ' precipitates nucleate on Al_3Zr precipitates. The orientation relationship between the precipitates is established to be: $(100)_{\theta'}//\{100\}_{Al_3Zr}$ :: $[001]_{\theta'}//\langle 001\rangle_{Al_3Zr}$.

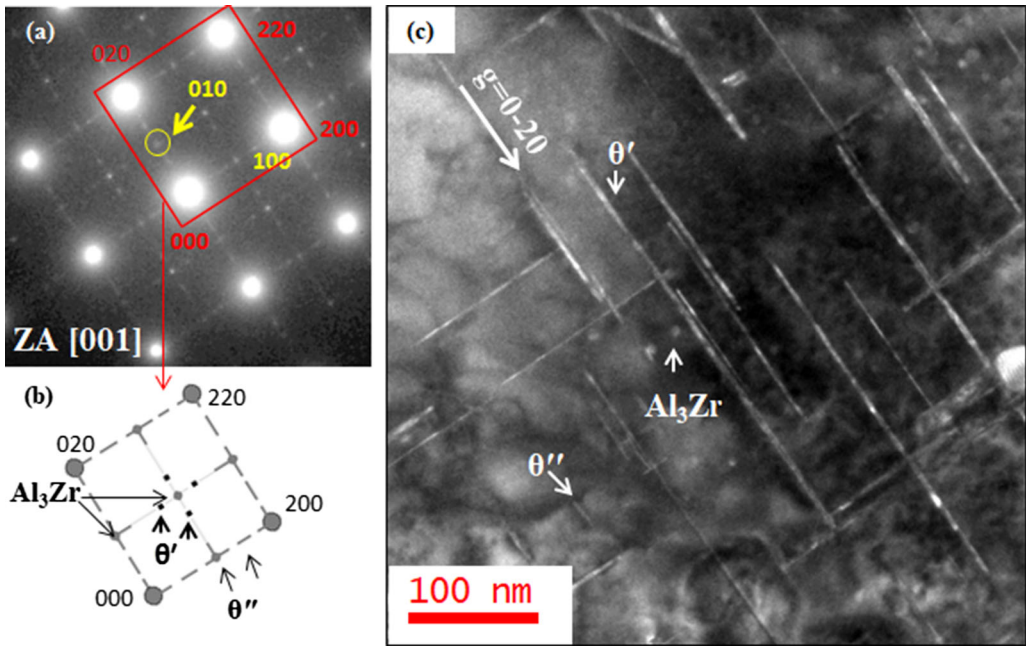

Fig. 6—2219NbZr alloy after peak aging at 473 K (200 °C). (*a*) SAD pattern along $[001]_{Al}$ zone axis, (*b*) schematic diagram of SAD pattern of enclosed area in (a), and (*c*) dark-field image corresponding to encircled superlattice ordered 010 spot.

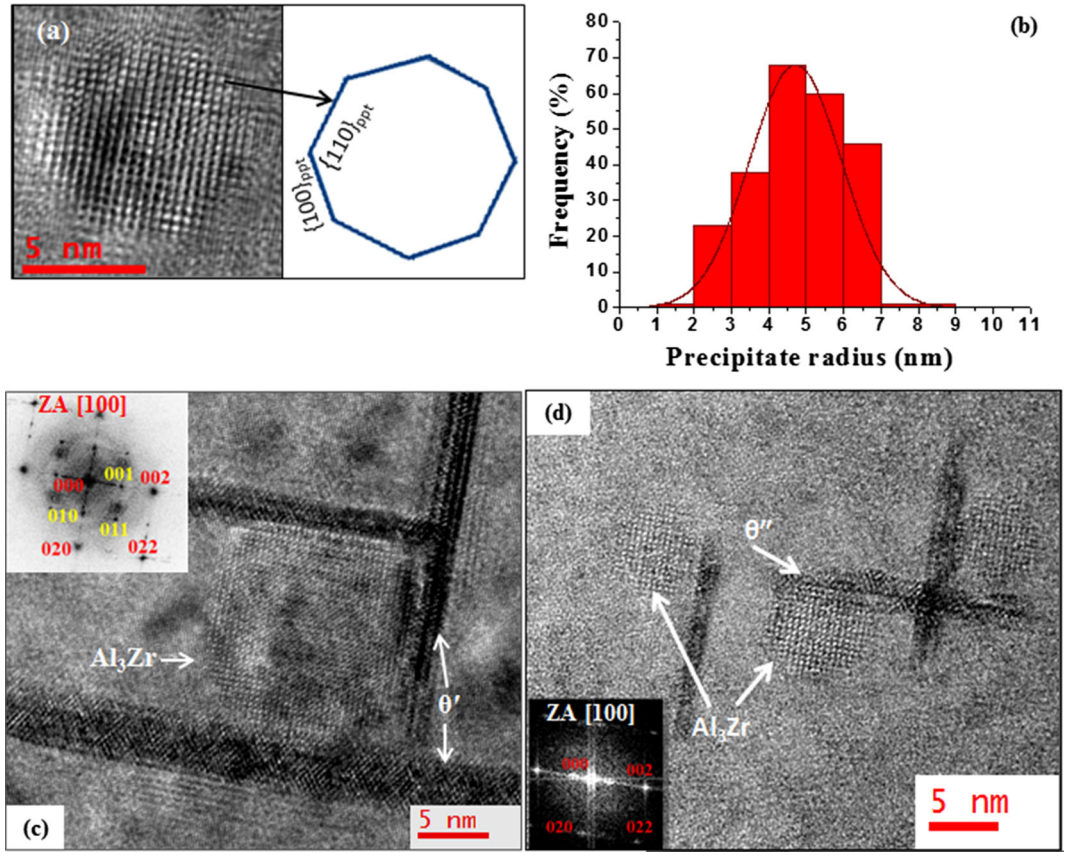

Fig. 7—2219NbZr alloy after peak aging at 473 K (200 °C). (*a*) inverse FFT image along $[100]_{Al}$ zone axis and schematic diagram of the precipitate, (*b*) size distribution curve of the Al_3Zr precipitates, (*c*) HRTEM image showing θ' precipitate nucleating on Al_3Zr, and (*d*) HRTEM image showing θ'' precipitates nucleating on Al_3Zr.

Figure 7(d) presents the HRTEM image near $[100]_{Al}$ zone axis, which shows θ'' precipitates along with Al_3Zr precipitates. The corresponding FFT in the inset shows that the streaks through the $\{200\}_{Al}$ reflection break up and give rise to distinct intensity maxima at $\{100\}_{Al}$, which confirms that these precipitates are θ''. The micrograph shows that Al_3Zr precipitates accompany one variant of θ'', which lies on (100) plane. Interestingly, the second kind of heterogeneous precipitation is only observed for Al_3Zr precipitates with smaller radius and without distinct facets. Figures 8(a) and (b) show the STEM images of the precipitates. Figure 8(a) shows θ'' precipitates along with Al_3Zr more clearly, whereas Figure 8(b) shows the overall microstructure. These micrographs corroborate the HRTEM results. Figure 8(c) shows a STEM mapping image of θ'' and the Al_3Zr precipitates. It confirms that the plate-like precipitates are Cu rich while the spherical precipitates are Zr rich.

Detailed analysis based on a large number of micrographs showed that θ'' and θ' precipitates nucleate on Al_3Zr/matrix interface. There are a few studies that report nucleation of θ' precipitate on pre-existing Al_3Zr particles. Galbraith *et al.*[40] reported heterogeneous nucleation of θ' on Al_3Zr particles in their study on Al-Cu-Li-Zr alloy. They rationalized that this kind of nucleation occurs when $\gamma^{c}_{\theta'/Al_3Zr} \leq \gamma_{\alpha/Al_3Zr} + \gamma_{\alpha/\theta'}$, where $\gamma^{c}_{\theta'/Al_3Zr}$ is the interfacial energy of θ'/Al_3Zr facet, γ_{α/Al_3Zr} is the energy of the curved α/Al_3Zr interface, and $\gamma_{\alpha/\theta'}$ is the energy of the curved α/θ' interface. It was observed that faceting influences the precipitation kinetics of plate-like precipitates on Al_3Zr by reducing the interfacial energy.[40] Heterogeneous nucleation of plate-like precipitates has also been reported by Kanno and Ou, and Itoh *et al.* for Al-Cu-Zr and Al-Cu-Zr-Li alloys,[41,42] and more recently by Chen *et al.*[8]

Length of θ'' and θ' precipitates were measured from a number of bright-field and STEM images and the thickness of the precipitates was measured from the HRTEM images. It was found that the θ'' precipitates have an average length of 21 ± 6.5 nm and an average thickness of 2.2 ± 0.5 nm. The average length of the θ' precipitates is 133 ± 60.3 nm and an average thickness is 4.2 ± 2.1 nm. It is observed that there is a distinct size difference between θ'' and θ' precipitates. The number density of θ'' and θ' precipitates are measured to be 1.2×10^{21} and 1.1×10^{21} m^{-3}. For 2219 alloy, solution treated at 808 K (535 °C) for 30 minutes and peak aged at 473 K (200 °C) for 20 hours, only θ' precipitates were observed. The average length of θ' precipitates is 127 ± 34 nm, average thickness is 5.1 ± 1.1 nm, and the number density is 1.01×10^{21} m^{-3}. Thus, the heterogeneous nucleation in 2219NbZr alloy leads to a finer average size and a higher number density of plate-shaped precipitates.

In Figure 5, it was observed that the alloy remains stable after 160 hours of aging. It implies that the coarsening kinetics of this alloy is very slow at 473 K

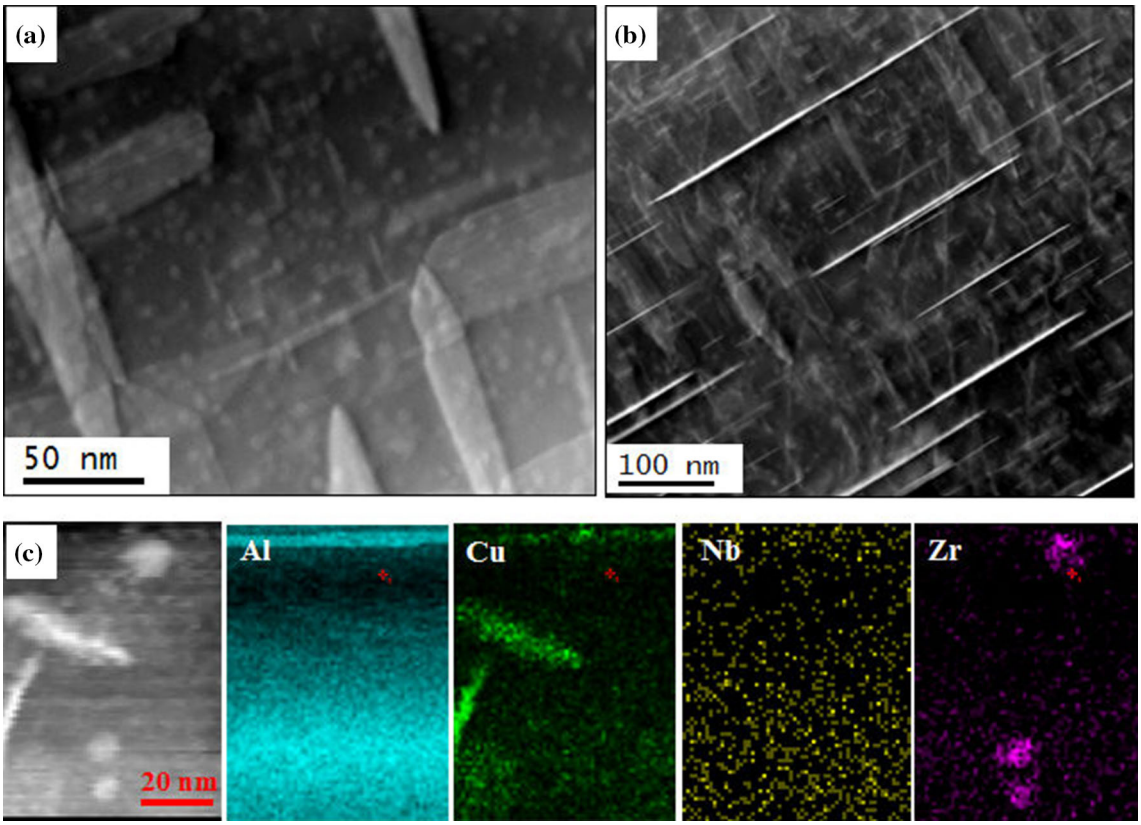

Fig. 8—2219NbZr alloy after peak aging at 473 K (200 °C). (*a*) and (*b*) STEM images of θ'' and θ' along with Al_3Zr precipitates, (*c*) representative STEM elemental mapping of θ'' along with Al_3Zr precipitates.

(200 °C). The slower growth and coarsening kinetics is attributed to the elastic strain energy minimization of the precipitates, which is demonstrated by the phase field simulation in the previous paper from our group.[38] The atom probe data in the previous paper also showed that some amount of Zr and Nb remained in the solid solution in the matrix.[38] The higher Zr and Nb solute-vacancy binding energy slows down the diffusion of Cu atoms in the matrix retarding the growth and coarsening of θ'' and θ' precipitates.

E. *Tensile Properties*

Tensile tests are performed after 10 hours of aging at 473 K (200 °C), *i.e.*, for the peak aged 2219NbZr alloy. The tensile properties at room temperature and 473 K (200 °C) are summarized in Table II. For a comparison, the tensile properties of the commercial 2219 alloy in the standard T851 temper at room temperature and 473 K (200 °C) are also presented in the same table. It is observed that the 2219NbZr alloy exhibits about 40 MPa higher 0.2 pct PS at room temperature as well as at 473 K (200 °C), though a lower elongation to fracture than the commercial 2219 alloy.

F. *Strengthening Mechanisms*

For the present study, the main contributors to strength for the 2219NbZr alloy are precipitation hardening and grain boundary strengthening. Precipitation strengthening is governed by Orowan bypassing or shearing mechanisms. The final microstructure consists of θ'', θ' and Al_3Zr precipitates. Coherent θ'' precipitates follow shearing mechanism, whereas θ' and Al_3Zr precipitates are bypassed by Orowan looping. For shearing mechanism, the factors that contribute to the increase in yield strength are coherency strengthening, modulus mismatch strengthening and order strengthening.

According to Brown and Ham,[43] the contribution due to modulus mismatch and order strengthening is negligible as compared to coherency strengthening. So, the strength increment due to θ'' precipitates is calculated using the following relation for coherency strengthening:

$$\tau_{\text{Shear}} = 4.1 \cdot G \cdot |\varepsilon^{3/2}| \cdot \left[\frac{V_v d_{\theta''}}{2b}\right]^{1/2}, \qquad [1]$$

where, τ_{shear} is the critical resolved shear stress (CRSS) to shear θ'' precipitates, volume fraction $V_v = \frac{N_v \pi d_{\theta''}^2 t_{\theta''}}{4}$, and lattice strain $\varepsilon = \frac{1}{3}\left(\frac{1+v}{1-v}\right)\delta$. The meaning of different symbols, the values used for the calculations and the values obtained from the calculations are given in Tables III and IV.

For the spherical $L1_2$ type Al_3Zr precipitates, CRSS for Orowan bypassing τ_{L1_2} is calculated from the following equation[44]:

$$\tau_{L1_2} = \frac{Gb}{2\pi\sqrt{1-v}} \cdot \frac{1}{\lambda} \cdot \ln\frac{\pi d_{L1_2}}{4b}, \qquad [2]$$

where, inter-particle spacing $\lambda = \frac{1.075}{\sqrt{N_v d_{L1_2}}} - \frac{\pi d_{L1_2}}{4}$ and d_{L12} is the diameter of the $L1_2$ type Al_3Zr precipitates.

To account for θ' precipitates, the modified Orowan model for precipitate thickness of 0.6–8 nm with random precipitate distribution, given by Nie and Muddle,[45] is used. The model states that the CRSS due to Orowan bypassing of θ' precipitates, $\tau_{\theta'}$, is given by:

$$\tau_{\theta'} = \frac{Gb}{2\pi\sqrt{1-v}} \left(\frac{1}{1.23\frac{1.030}{\sqrt{N_v d_{\theta'}}} - \frac{\pi d_{\theta'}}{s} - 1.061 t_{\theta'}}\right) \ln\frac{0.981\sqrt{d_{\theta'} t_{\theta'}}}{b}. \qquad [3]$$

Total strength increment due to the presence of all the precipitates is determined using the following ad hoc superposition law[46]:

$$\tau_{\text{ppt}}^{1.4} = \tau_{\text{shear}}^{1.4} + \left[\left(\tau_{L1_2}^2 + \tau_{\theta'}^2\right)^{0.5}\right]^{1.4}, \qquad [4]$$

where τ_{ppt} is the total critical resolved shear stress (CRSS) due to all the precipitates observed in the microstructure. The calculated values are listed in Table IV.

Grain boundary strengthening is calculated using the Hall–Petch equation.[47]

$$\sigma_{\text{gb}} = \sigma_i + K_i d^{-m}, \qquad [5]$$

where σ_{gb} denotes the yield strength due to grain boundaries, σ_{i} denotes the yield strength for pure Al with infinite grain size, d is the average grain size for the alloy, and m is the exponent for grain boundary strengthening. After evaluating the strength contribution due to the precipitates and grain boundaries, the total theoretical yield strength, σ_{total}, can be calculated as follows[48]:

Table II. Tensile Properties of the 2219NbZr Alloy Peak Aged at 200 °C and 2219-T851 Alloy

	0.2 Pct Proof Stress (MPa)		UTS (MPa)		Pct Elongation	
	2219NbZr	2219-T851	2219NbZr	2219-T851	2219NbZr	2219-T851
RT	409 ± 10	352 ± 18	530 ± 32	440 ± 21	2 ± 0.2	9 ± 1
200 °C	252 ± 22	217 ± 28	306 ± 12	245 ± 23	5.3 ± 0.4	19 ± 2

Table III. Notations and Values of Different Symbols Used in the Strengthening Mechanism Calculations

Symbol	Description	Value
G	shear modulus of the aluminum matrix phase	28 GPa
ε	lattice strain	6×10^{-3}
δ	lattice misfit strain at the particle–matrix interface for disk-shaped precipitates	0.009
b	magnitude of the Burgers vector for aluminum	0.286 nm
N_v	precipitate number density per unit volume of the matrix phase	refer Table IV
d_{par}	length of plate-shaped and diameter of spherical precipitates	refer Table IV
t_{par}	thickness of plate-shaped precipitates	refer Table IV
υ	Poisson's ratio	1/3
σ_i	yield strength for pure Al with infinite grain size	16 MPa
K_i	Hall–Petch constant	0.065 MPa $m^{1/2}$
d	grain size	30 μm
m	exponent for grain boundary strengthening	1/2
M	Taylor factor	3

Table IV. The Values Calculated from the Obtained Microstructure

	d_{par} (nm)	t_{par} (nm)	λ (nm)	N_v (1/nm^3)	τ_{L12} (MPa)	$\tau\theta''$ (MPa)	$\tau_{\theta'}$ (MPa)
Al_3Zr	9.4	—	92	12.37×10^{-6}	55	—	—
θ''	21	2.2	—	1.21×10^{-6}	—	10	—
θ'	133	4.2	—	1.10×10^{-6}	—	—	135

Table V. Theoretical Yield Strength Calculation and Experimental 0.2 Pct PS Value for the Peak Aged Sample

Strength Contribution (MPa)	Grain Boundaries σ_{gb}	Al_3Zr, θ'' and θ' Precipitates $\sigma_{\text{ppt}} = M \cdot \tau_{\text{ppt}}$	Total Calculated Yield Strength σ_{total}	Experimental 0.2 Pct PS
2219NbZr	28	446	474	409

$$\sigma_{\text{total}} = \sigma_{\text{gb}} + M \cdot \tau_{\text{ppt}}. \quad [6]$$

The calculated strength values are reported in Table V. Based on the theoretical calculation, the theoretical total strength comes out to be 474 MPa, whereas the experimentally obtained value is 409 MPa.

IV. CONCLUSIONS

A small amount of Zr and Nb are added to 2219 alloy and the alloy is processed by a novel three-stage heat treatment developed by our group. During the first stage of aging, homogeneously dispersed nanometer-sized $L1_2$ ordered Al_3Zr precipitates are formed. These precipitates are spherical in nature and their average radius is about 2.3 ± 0.5 nm. Subsequently, solution treatment at 808 K (535 °C) for 30 minutes leads to a change in size distribution of Al_3Zr precipitates. At this temperature the average size (radius) of the precipitates increases to 4.7 ± 1.4 nm. A distinct facet formation is observed on {100} and {110} planes of the Al_3Zr precipitates depending on the size. Faceted morphology of the Al_3Zr particles facilitates heterogeneous nucleation of θ'' or θ' precipitates on them. Room temperature and 473 K (200 °C), 0.2 pct proof stress is improved by about 40 MPa as compared to the commercial 2219-T851 alloy, though ductility is lowered. A theoretical estimate of different strength contributions is made. The strength essentially comes from θ'', θ', and Al_3Zr precipitates, and, to a smaller extent, from fine grain size.

REFERENCES

1. E. Hornbogen and E.A. Starke, Jr.: *Acta Metall. Mater.*, 1993, vol. 41, pp. 1–16.
2. J.W. Martin: *Precipitation Hardening*, 2nd ed., Butterworth-Heinemann, Oxford, 1998.
3. K.E. Knipling, D.C. Dunand, and D.N. Seidman: *Z. Metallkd.*, 2006, vol. 97, pp. 246–65.
4. K.E. Knipling, D.C. Dunand, and D.N. Seidman: *Metall. Mater. Trans. A*, 2007, vol. 38A, pp. 2552–63.
5. K.E. Knipling, D.C. Dunand, and D.N. Seidman: *Microsc. Microanal.*, 2007, vol. 13, pp. 503–16.
6. S. Pogatscher, H. Antrekowitsch, M. Werinos, F. Moszner, S.S.A. Gerstl, M.F. Francis, W.A. Curtin, J.F. Löffler, and P.J. Uggowitzer: *Phys. Rev. Lett.*, 2014, vol. 112, pp. 225701–705.
7. R.K.W. Marceau, G. Sha, R. Ferragut, A. Dupasquier, and S.P. Ringer: *Acta Mater.*, 2010, vol. 58, pp. 4923–39.

8. B.A. Chen, L. Pan, R.H. Wang, G. Liu, P.M. Cheng, L. Xiao, and J. Sun: *Mater. Sci. Eng. A*, 2011, vol. 530, pp. 607–17.
9. F. Wang, Z. Liu, D. Qiu, J.A. Taylor, M.A. Easton, and M.-X. Zhang: *Acta Mater.*, 2013, vol. 61, pp. 360–70.
10. W. Feng, Q.I.U. Dong, Z. Liu, J. Taylor, M. Easton, and M. Zhang: *Trans. Nonferrous Met. Soc. China*, 2014, vol. 24, pp. 2034–40.
11. M. Easton and D. Stjohn: *Metall. Mater. Trans. A*, 1999, vol. 30A, pp. 1613–23.
12. B.S. Murty, S.A. Kori, and M. Chakraborty: *Int. Mater. Rev.*, 2002, vol. 47, pp. 3–29.
13. Y. Zhang, C. Bettles, and P.A. Rometsch: *J. Mater. Sci.*, 2013, vol. 49, pp. 1709–15.
14. J. S. Vetrano, S. M. Bruemmer, and I. M. Robertson: *MRS Online Proceedings Library Archive*, 1995, 404.
15. J.S. Vetrano, S.M. Bruemmer, L.M. Pawlowski, and I.M. Robertson: *Mater. Sci. Eng. A*, 1997, vol. 238, pp. 101–07.
16. K. Kannan, J.S. Vetrano, and C.H. Hamilton: *Metall. Mater. Trans. A*, 1996, vol. 27A, pp. 2947–57.
17. J. Murray, A. Peruzzi, and J.P. Abriata: *J. Phase Equilibria*, 1992, vol. 13, pp. 277–91.
18. K.E. Knipling, D.C. Dunand, and D.N. Seidman: *Acta Mater.*, 2008, vol. 56, pp. 114–27.
19. M.S. Zedalis and M.E. Fine: *Metall. Mater. Trans. A*, 1986, vol. 17A, pp. 2187–98.
20. S. Z. Han, S. C. Chung, H. M. Lee: (1995). *Metall. Mater. Trans. A,* 1995, vol 26A, pp 1633–39.
21. V.R. Parameswaran, J.R. Weertman, and M.E. Fine: *Scr. Metal.*, 1989, vol. 23, pp. 147–50.
22. K.E. Knipling, D.C. Dunand, and D.N. Seidman: *Acta Mater.*, 2008, vol. 56, pp. 1182–95.
23. E. Nes: *Acta Metall.*, 1972, vol. 20, pp. 499–506.
24. R. Srinivasan: *Acta Crystallogr. A*, 1992, vol. 48, pp. 917–18.
25. K.S. Vecchio and D.B. Williams: *Acta Metall.*, 1987, vol. 35, pp. 2959–70.
26. S. Srinivasan, P.B. Desch, and R.B. Schwarz: *Scr. Metal. Mater.*, 1991, vol. 25, pp. 2513–16.
27. K.E. Knipling and D.C. Dunand: *Scr. Mater.*, 2008, vol. 59, pp. 387–90.
28. L. F. Mondolfo: *Aluminum alloys: Structure and properties*, London-Boston Butter Worths & Co Ltd, 1976.
29. C. Colinet, A. Pasturel, D.N. Manh, D.G. Pettifor, and P. Miodownik: *Phys. Rev. B*, 1997, vol. 56, pp. 552–65.
30. R. Vilar, O. Conde, and S. Franco: *Intermetallics*, 1999, vol. 7, pp. 1227–33.
31. A. B. Pandey: *US patent*, 2011, patent no. 8,002,912 B2.
32. E. Nes and H. Billdal: *Acta Metal.*, 1977, vol. 25, pp. 1039–46.
33. M.S. Chuang and G.C. Tu: *Scr. Metal. Mater.*, 1995, vol. 33, pp. 1999–2005.
34. Y.C. Chen, M.E. Fine, and J.R. Weertman: *Acta Metal. Mater.*, 1990, vol. 38, pp. 771–80.
35. M.S. Zedalis and M.E. Fine: *Scr. Metal.*, 1983, vol. 17, pp. 1247–51.
36. M. S. Zedalis and M. E. Fine " Metal Trans A, 1986, vol. 17, pp 2187-2198.
37. S. K. Makineni: *Indian Institute of Science*, Ph.D thesis, Bangalore, India 2015.
38. S.K. Makineni, S. Sugathan, S. Meher, R. Banerjee, S. Bhattacharya, S. Kumar, and K. Chattopadhyay: *Sci Rep.*, 2017, https://doi.org/10.1038/s41598-017-11540-2.
39. S. K. Makineni, S Mondol, S. Suwas, S. Kumar, K. Chattopadhyay: Indian patent, WO2015121723 A1, 2015, US Patent 15/118670, 2016.
40. J.M. Galbraith, M.H. Tosten, and P.R. Howell: *J. Mater. Sci.*, 1987, vol. 3, pp. 2227–36.
41. M. Kanno and B. Ou: *Mater. Tarns. JIM*, 1991, vol. 32, pp. 445–50.
42. G.C.U.I.Q. Itoh, Q. Cui, and M. Kanno: *Mater. Sci. Eng. A*, 1996, vol. 211, pp. 128–37.
43. L.M. Brown and R.K. Ham: in *Strengthening Methods in Crystals*, A. Kelly and R.B. Nicholson, eds., Wiley, New York, 1971.
44. A.W. Zhu, A. Csontos, and E.A. Starke: *Acta Mater.*, 1999, vol. 47, pp. 1713–21.
45. J.F. Nie and B.C. Muddle: *Acta Mater.*, 2008, vol. 56, pp. 3490–501.
46. D.L. Gilmore and E.A. Starke: *J. Metall. Mater. Trans. A*, 1997, vol. 28A, pp. 1399–1415.
47. G.E. Dieter: *Mechanical Metallurgy*, 3rd ed., McGraw Hill, New York, 1986.
48. M. Dixit, R.S. Mishra, and K.K. Sankaran: *Mater. Sci. Eng. A*, 2008, vol. 478, pp. 163–72.